

8-2016

Haptic Feedback Effects on Human Control of a UAV in a Remote Teleoperation Flight Task

Evan Joseph Sand

Clemson University, esand@clemson.edu

Follow this and additional works at: https://tigerprints.clemson.edu/all_theses

Recommended Citation

Sand, Evan Joseph, "Haptic Feedback Effects on Human Control of a UAV in a Remote Teleoperation Flight Task" (2016). *All Theses*. 2440.

https://tigerprints.clemson.edu/all_theses/2440

This Thesis is brought to you for free and open access by the Theses at TigerPrints. It has been accepted for inclusion in All Theses by an authorized administrator of TigerPrints. For more information, please contact kokeefe@clemson.edu.

HAPTIC FEEDBACK EFFECTS ON HUMAN CONTROL OF A UAV IN A REMOTE TELEOPERATION FLIGHT TASK

A Thesis
Presented to
the Graduate School of
Clemson University

In Partial Fulfillment
of the Requirements for the Degree
Master of Science
Mechanical Engineering

by
Evan Joseph Sand
August 2016

Accepted by:
Dr. Yue “Sophie” Wang, Committee Chair
Dr. John Wagner
Dr. Mohammed Daqaq

Abstract

The remote manual teleoperation of an unmanned aerial vehicle (UAV) by a human operator creates a human-in-the loop system that is of great concern. In a remote teleoperation task, a human pilot must make control decisions based upon sensory information provided by the governed system. Often, this information consists of limited visual feedback provided by onboard cameras that do not provide an operator with an accurate portrayal of their immediate surroundings compromising the safety of the mobile robot. Due to this shortfall, haptic force feedback is often provided to the human in an effort to increase their perceptual awareness of the surrounding world.

To investigate the effects of this additional sensory information provided to the human operator, we consider two haptic force feedback strategies. They were designed to provide either an attractive force to influence control behavior towards a reference trajectory along a flight path, or a repulsive force directing operators away from obstacles to prevent collision. Subject tests were conducted where human operators manually operated a remote UAV through a corridor environment under the conditions of the two strategies. For comparison, the conditions of no haptic feedback and the linear combination of both attractive and repulsive strategies were included in the study. Experimental results dictate that haptic force feedback in general (including both attractive and repulsive force feedback) improves the average distance from surrounding obstacles up to 21%. Further statistical comparison of repulsive and attractive feedback modalities reveal that even though a repulsive strategy is based directly on obstacles, an attractive strategy towards a reference trajectory is more suitable across all performance metrics.

To further examine the effects of haptic aides in a UAV teleoperation task, the behavior of the human system as part of the control loop was also investigated. Through a novel device placed

on the end effector of the haptic device, human-haptic interaction forces were captured and further analyzed. With this information, system identification techniques were carried out to determine the plausibility of deriving a human control model for the system. By defining lateral motion as a one-dimensional compensatory tracking task the results show that general human control behavior can be identified where lead compensation is invoked to counteract second-order UAV dynamics.

Acknowledgments

First and foremost I would like to thank my advisors Dr. Yue Wang and Dr. John Wagner. Their continued support and direction throughout my time as a graduate student has driven me to only accept my best and have proved as invaluable resources in my research efforts. I am also thankful to my fellow students in our research group for their knowledge and support. I would especially like to thank Hamed Saeidi for his never yielding effort to help me reach my goals. His clarity, advice and comfort in even the most desperate of times will forever be a testament to his character and leadership ability.

Finally, this achievement could not have come to fruition without the love, care and financial contribution of my family and friends to which I am forever in debt. Last but not least I would like to thank my wife and children for their support during my time as a research student. To them I owe the world and intend to deliver.

Table of Contents

Title Page	i
Abstract	ii
Acknowledgments	iv
List of Tables	vii
List of Figures	viii
1 Introduction	1
1.1 Background on UAV Haptic Feedback	2
1.2 Human System Identification	4
1.3 Overview	5
2 UAV Haptic Force Feedback	7
2.1 UAV Dynamics	7
2.2 Haptic Device	8
2.3 Haptic Feedback	8
3 UAV Pilot Model Identification	14
3.1 Crossover Model	15
3.2 Operator Identification	17
4 Experimental Design	20
4.1 Physical Set Up	20
4.2 Human Force Sensor	22
4.3 Procedure	26
5 Performance Results	27
5.1 Flight Performance Metrics	27
5.2 Operator Workload Metrics	28
5.3 Simulation Study	28
5.4 Real Study	33
6 Human Identification Results	37

7 Conclusions and Discussion	41
Appendices	43
A Participant Demographics	44
Bibliography	45

List of Tables

3.1	Extended Crossover Model	16
4.1	Average constant coefficients	24
5.1	Performance metrics for simulated study	29
5.2	Performance metrics of real study	34

List of Figures

2.1	Weighting functions for attractive and repulsive force rendering.	10
2.2	Gradient of force magnitudes along flight course.	13
3.1	Control diagram for compensatory tracking	14
3.2	Control diagram including haptic aid.	15
3.3	Human perception of error	17
4.1	Remote workspace providing only visual and haptic interfaces.	20
4.2	UAV flight track	21
4.3	Force sensor array to record human-haptic interaction forces.	23
4.4	Calibrated human-haptic force	25
5.1	Means of performance metrics with higher vertical values representing more favorable values for NF (yellow), RF (red), AF (blue) and RF+AF (green).	30
5.2	(a,c,e) Haptic force distribution represented in haptic device workspace; (b,d,f) Total haptic force over time with the horizontal line representing the average force.	31
5.3	Medians and interquartile ranges of subjective metrics with outliers (+). PQ represents performance questionnaire and HA represents haptic acceptance.	32
5.4	Means of performance metrics for real flight. NF (yellow), RF (red), AF (blue) and RF+AF (green).	35
5.5	Medians and interquartile ranges of subjective metrics with outliers (+). PQ represents performance questionnaire and HA represents haptic acceptance.	36
6.1	Estimated open-loop frequency response functions for all feedback conditions.	37
6.2	Means and 95% confidence intervals of the crossover frequency values.	38
6.3	Mean UAV frequency response	39
6.4	Mean human response estimates	40

Chapter 1

Introduction

The rise in commercially available unmanned aerial vehicles (UAV), has prompted wide interest in their applicational use. Until recent years, these robots have been limited to militaristic tasks and have proven as an acceptable alternative to direct human involvement [1]. With this increased availability, their roles in both recreational and industrial applications have expanded tremendously [2]. Although small UAVs have limited abilities due to their lack of onboard manipulators, their ability to traverse harsh terrains as well as cramped and cluttered environments make them better suited for certain applications over ground based mobile robots [3][4]. They serve as an ideal tool for general survey and surveillance tasks over ground based mobile robots through their increased maneuverability and vertical workspace. Through remote teleoperation, UAV's can additionally be placed in environments that do not warrant human presence and improve human safety.

One major drawback of remote teleoperation is a limited perception of the extended environment due to visual constraints. To achieve improved safety for the mobile robot during a flight task, the operator must be provided with information about the flight environment beyond the visual feedback provided by onboard cameras [5]. In an effort to provide this information to the operator, specific algorithms and strategies are implemented to construct haptic cues based upon several environmental and UAV state parameters.

Numerous feedback structures have been introduced throughout literature that have proven to enhance flight performance. They have done so by focusing on collision avoidance [6] and/or op-

timal trajectory adherence [7]. Collision avoidance provides the operator with a repulsive force that opposes motion in the direction of an obstacle. Trajectory adherence provides instead an attractive force that attempts to guide the vehicle towards a reference trajectory.

While both collision avoidance and trajectory adherence feedback strategies have shown an increase in flight performance, they have consistently proven themselves superior over non-haptic flight alone. Currently, there exists no extensive literature for the comparison of these paradigms with respect to each other. One of the aims of this work is to examine the relative performance of these paradigms to propose the most suitable model for human-operated UAV flight.

Additionally, in order to further improve human performance in remote teleoperation flight tasks, information on human control is necessary [8]. With the addition of haptic force feedback, performance may improve but with degradation of user comfort in the form of increased workload. Proper haptic tuning is therefore paramount to improve human acceptance of the additional sensory information so that workload is reduced without sacrificing human control authority to simply improve performance [9]. For this reason, a method for human control system identification is a necessity.

1.1 Background on UAV Haptic Feedback

Remote haptic teleoperation of mobile robots typically consists of three essential blocks: an operator interfacing a haptic device (Master), a ground station providing bilateral communication (Channel) and a mobile robot (Slave) [10] [11]. Using this system for manual teleoperation, there currently exists three groups of haptic cues that are typically used as force feedback (FFB) sources in conventional teleoperation systems. The first is based upon the mismatch between the commanded input from the master and the output of the slave (master-slave tracking error). The second is a force rendered according to the external environment with respect to the slave and the third is a combination of the first two [12]. This study will focus on the second case according to the idea of artificial force fields (AFF).

The design of AFFs are based heavily on the principal that obstacles exert a virtual repul-

sive haptic cue while targets or goals provide a virtual attractive haptic cue [13]. The majority of work with AFF feedback algorithms utilize a three degree-of-freedom (DoF) haptic device to control a UAV in Euclidean space and therefore a vector approach is used to calculate a haptic force. Vectors are produced based upon two main variables in a UAV flight task. The first is the current state of the vehicle including the current position, orientation and velocity. The second is the external environment surrounding the mobile robot such as obstacles. Repulsive collision avoidance algorithms use the distance between the UAV and an obstacle and/or the current velocity to produce a haptic force vector [14]. For these, a vector pointing from each obstacle to the vehicle is produced with a magnitude associated to its distance or chance of collision. After each obstacle has been provided with a vector, their components are added together to create an overall haptic force sent to the master device. In [13, 15, 16], the magnitude of each vector is found by combining the obstacles distance with the vehicles velocity and maximum deceleration. In [17] the authors also account for the velocity of dynamic obstacles. While the respective velocity of the vehicle and obstacles can contribute in collision avoidance, other papers such as [18], derive the haptic force from simply the distance to an obstacle.

A feedback scheme providing collision avoidance based on obstacles themselves would be a logical choice for cluttered environments. However, if the vehicle is in an environment with a large number of obstacles there can arise an issue due to the constant changing of obstacles in the robot workspace and provide the operator with an unwarranted jerking response from the haptic device making teleoperation difficult. Also, obstacles can be located in a geometric pattern (such as a corner) that, when combined, can cancel and provide an incorrect haptic force to the operator. For this case a trajectory adherence feedback scheme may be more appropriate to provide a smooth response to the operator.

For attractive path following feedback algorithms, the same vector approach can be used to guide a UAV back to a planned trajectory. In this case the planned trajectory can be thought of as a target point for the UAV to maneuver to [7]. While these two feedback paradigms differentiate in their function of repulsion and attraction, their force magnitudes are also inversely related. Repulsive forces increase as the relational distance decreases while the attractive forces increase as the

relational distance increases.

1.2 Human System Identification

To better understand the human role in UAV manual control and the effects that haptic feedback has on their control behavior, system identification is a necessity [19] [20]. This is important as human dynamic characteristics directly influence the performance of the human-robot system under manual control because they are defined as a part of the overall system [21].

The human operator is an example of a nonlinear biologically dynamic system but can be approximated as a quasi-linear time-invariant model along with an associated remnant signal accounting for nonlinear behavior [22]. In a manual-control tasks a human operator bases their control actions upon perceptual information provided by the governed system. One of the earliest studies into human control that has encapsulated the dynamic relationship between that of a human operator and controlled element is the pilot crossover model of McRuer et al. [23]. The theories of the aforementioned detail that a human operator is consistent in how they alter their behavior based upon the dynamics of the system they are controlling [24]. Therefore, as the human control is specific to the system they are controlling, it is equally important that identification should be conducted directly on the system that they are using [25]. More detail on the specifics of the crossover model will be discussed in subsequent chapters of this work.

According to [26], the human can be split into an internal subsystem using both feedforward and feedback action based upon the signal presented to the human. They state that a feedforward action is implemented when predictable target signals are presented while feedback control is dependent on the tracking error signal alone. In [27], the authors outline that human control strategies can be categorized into three types based upon human perception of the task. The first is compensatory control. Compensatory control is where the human only has a perceived or provided tracking error available to them and they rely heavily on the feedback control loop providing this information. In pursuit control or also known as preview, the operator uses past experiences or knowledge to predict future outcomes. Pursuit tracking is often associated with an additional feedforward action

evoked by the operator due to their prediction of where a target position should be. Lastly, precognitive control is where a human operator would have complete knowledge about system dynamics and future outcomes. From this, the human control model can be analyzed as a single block of a feedback control loop or the sum of several internal blocks contributing to control actions.

Through literature review, almost all past research on related human system identification has been done in a simulated setting with a simple tracking task. The tracking task involves a visual moving target signal on a screen that the human attempts to follow through the use of an input device controlling a virtual robot to minimize tracking error. Where the studies differ is in the method by which the target signal is presented. For some [28][29][30][31], the reference signal is only presented to the operator at the current moment in time modeling compensatory control. In others [31][32], a preview of the reference signal is presented to study pursuit control. To the author's knowledge, none of the the simulated system identification pertained to UAV flight, therefore the control of a remote UAV can most closely be related to that of piloting an aircraft where much study has been conducted. In [33], the pilot control of an aircraft is defined as a compensatory control task as the human operator only visualizes the tracking error of pitch dynamics. For this and several similar studies [34][32][26], the human is presented with a screen representing the pitch error with or without a horizon where the dynamics of the system are closely modeled to that of an actual airplane or helicopter system.

1.3 Overview

The works presented here have all contributed to human performance in a manual control task. The summation of the presented research on haptic force feedback and human control system identification can lead to proper design of a remote teleoperation flight task of a UAV with supportive haptic force feedback. Based upon literature review, many real life experiments have been conducted for UAV collision avoidance but as of yet no non-simulation human identification has been compiled. More specifically, full scale human pilot models for control of quadrotor UAV's has yet to be conceived. The purpose of this study is an attempt to bridge this gap and prove the

plausibility of human system identification for real tests in a two-dimensional environment so that full dynamics of the true system can be captured.

To examine the differences in repulsive and attractive haptic force feedback (FFB) as well as to examine human control behavior under their influence, a course was created for a human operator to remotely control a quadrotor UAV under the direction of the presented modalities to objectively compare the performance of each. Chapter 2 describes the system dynamics of a UAV interfaced by a haptic device. It also includes a description of the algorithms chosen to produce haptic force feedback. Chapter 3 details how to accurately estimate a human pilot model. Chapter 4 describes in detail the physical set up of the experimental system including the design of a sensor array to measure human interaction forces as well as the procedure of the experiments. Chapter 5 shows the performance results of both a simulation and full-scale test. Chapter 6 details the results of human pilot model identification. Finally conclusions regarding the work as a whole are presented in Chapter 7.

Chapter 2

UAV Haptic Force Feedback

2.1 UAV Dynamics

This study considers the use of a UAV quadrotor capable of hover and near-hover flight with an associated body frame, \mathcal{B} , that is related to the inertial frame, \mathcal{W} , by the rotational matrix defined as $R_{\mathcal{B}}^{\mathcal{W}}$. Here, $[\vec{X}_r, \dot{\vec{X}}_r, \ddot{\vec{X}}_r] \in \mathcal{W}$ are the UAV position, velocity and acceleration respectively with $\omega \in \mathcal{B}$ the angular velocity. Let M and I represent the total mass of the UAV and the inertia of the body respectively. Assuming the UAV as a rigid body its dynamics are obtained using the Newton-Euler formalism [35] as

$$M\ddot{\vec{X}}_r = R_{\mathcal{B}}^{\mathcal{W}}F \quad (2.1)$$

$$\dot{R}_{\mathcal{B}}^{\mathcal{W}} = R_{\mathcal{B}}^{\mathcal{W}}\omega_{\times} \quad (2.2)$$

$$\mathbf{I}\dot{\omega} = -\omega \times \mathbf{I}\omega + \Gamma \quad (2.3)$$

where ω_{\times} represents a skew-symmetric matrix such that $\omega_{\times}\dot{\vec{x}}_r = \omega \times \dot{\vec{x}}_r$. The terms Γ , and $F \in \mathcal{B}$ are the external torque and force inputs respectively.

2.2 Haptic Device

A haptic device with 3-DoF to send rate control commands (velocity) to the UAV was utilized. The position of the end effector $\vec{q} = (q_1, q_2, q_3)^T \in \mathbb{R}^3$ in reference to a zero point in its workspace provides these inputs to the system. The haptic device is a fully actuated system modeled by the Euler-Lagrange equation

$$m(q)\ddot{q} + C(q, \dot{q})\dot{q} + G(q) = F_h + U_h \quad (2.4)$$

where $m(q)$ is the mass matrix of the device, $D(q) > 0$ is the damping matrix, $C(q, \dot{q})$ is the Coriolis matrix and $G(q)$ is the gravitational force. The term U_h is the external force provided by the human operator and F_h is the FFB from the device.

2.3 Haptic Feedback

This section presents three FFB algorithms to achieve desired goals of repulsive obstacle avoidance, attractive trajectory adherence and a linear combination of both. The FFB algorithms resemble components of the one proposed in [7] but with adaptation to this particular case of study where the attractive and repulsive forces are resolved independently without the use of a timing law and trajectory regeneration is neglected.

2.3.1 Repulsive Haptic Feedback for Obstacle Avoidance

For the obstacle based repulsive FFB a total force vector is calculated using contributions of each obstacle in the local UAV workspace. This force vector is normalized as a factor of the maximum force that the haptic device can provide. For example, if the UAV hits an obstacle, the haptic device would be providing the maximum force while no obstacles in the local workspace would provide no force. Let $\vec{f}_{o,i} \in \mathbb{R}$, $i = 1, 2, \dots, n$ defined by the function: $\vec{f}_{o,i} = g_r(\vec{X}_r, \vec{X}_{o,i})$ be the force vector for n obstacles located within the local UAV workspace. Here, g_r is a function of two parameters: $\vec{X}_r \in \mathcal{W}$, representing position of the UAV and $\vec{X}_{o,i} \in \mathcal{W}$ the position of the i^{th} obstacle.

Respectively, $\vec{X}_r = (x_r, y_r, z_r)$, $\vec{X}_{oi} = (x_{oi}, y_{oi}, z_{oi})$. For each obstacle, a weighting factor, $\lambda(d_i)$, is calculated with $d_i = \|\vec{X}_r - \vec{X}_{oi}\| - r_{uav}$ being the Euclidean distance between the obstacle and UAV with radius, r_{uav} . Defining r_w as the radius of the UAV workspace, the weighting factor is found according to

$$\lambda(d_i) = \begin{cases} e^{(-d_i/r_w^2)} & \text{if } d_i \leq r_w \\ 0 & \text{if } d_i > r_w \end{cases}, \quad i = 1, 2, \dots, n \quad (2.5)$$

Using the associated unit vector \hat{d}_i , a new unit vector pointing from the obstacle to the UAV in the body frame, \mathcal{B} , is computed as $\hat{\delta}_i = R_{\mathcal{W}}^{\mathcal{B}} \cdot \hat{d}_i$. Each individual obstacle force vector is now calculated according to

$$\vec{f}_i = \lambda(d_i) \cdot \hat{\delta}_i \quad (2.6)$$

Combining n obstacles yields an overall repulsive force vector, \vec{F}_r .

$$\vec{F}_r = \begin{cases} 0 & \text{if } n = 0 \\ \vec{f}_i & \text{if } n = 1 \\ \frac{\sum_{i=1}^n \vec{f}_i}{\sum_{i=1}^n \lambda(d_i)} & \text{if } n > 1 \end{cases} \quad (2.7)$$

Finally, the repulsive FFB is sent to the haptic controller in the \mathcal{H} frame is according to

$$\vec{F}_h = k_{max}(R_{\mathcal{B}}^{\mathcal{H}} \cdot \vec{F}_r) \quad (2.8)$$

where k_{max} is a positive scaling factor representing the maximum force of the haptic device.

2.3.2 Attractive Haptic Feedback for Trajectory Adherence

For attractive FFB, the current position of the UAV, \vec{X}_r , is paired with the position of a point on a predefined trajectory. Let $S(x, y, z) \in \mathbb{R}$ represent an optimal trajectory for the UAV to fly. This trajectory is produced using a 4th order b-spline consisting of control points located at the midpoint between adjacent obstacles along the corridor path [36]. To compute an attractive force to this path,

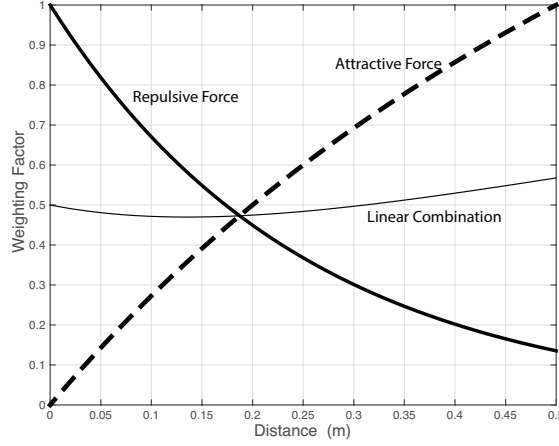


Figure 2.1: Weighting functions for attractive and repulsive force rendering.

define $\vec{F}_a \in \mathbb{R}$ to be the force vector associated with pulling the UAV back towards the preferred path. The force function is: $\vec{F}_a = g_a(\vec{X}_a, \vec{X}_r)$ where g_a is a function of two parameters: $\vec{X}_r \in \mathcal{W}$ defined above and $\vec{X}_a \in \mathcal{W}$, the position of a point on the reference trajectory. More specifically, $\vec{X}_a = (x_a, y_a, z_a)$. Unlike the repulsive force above, where multiple obstacles are found in the UAV's workspace, this approach contains only one point and must have a different weighting function. However, to be consistent for the purposes of comparison between the two paradigms a weighting function with an inverse shape was selected. For the attractive case, $d_a = \|\vec{X}_r - \vec{X}_a\|$ represents the Euclidean distance between the UAV and reference point. The lack of compensation for the radius of the UAV here is because the current state of the robot is measured at the UAV center of mass (COM). Elaborating, the position of the UAV and an obstacle cannot be the same as a collision would have occurred at a distance of r_{uav} from the COM. For the attractive case however, the UAV COM is desired to coincide with a virtual reference point and compensation is unnecessary. The attractive sigmoidal weighting function is prescribed as

$$\vec{F}_a = \begin{cases} 1 & \text{if } d_a > r_w \\ \left[\frac{d_a}{1+d_a} + \frac{d_a}{r_w(1+d_a)} \right] \cdot \hat{\delta}_a & \text{if } d_a \leq r_w \end{cases} \quad (2.9)$$

where $\hat{\delta}_a$ is the unit vector pointed from the UAV to the reference point translated to the \mathcal{B} frame as $\hat{\delta}_a = R_{\mathcal{W}}^{\mathcal{B}} \cdot \hat{d}_a$. The second term in equation (2.9) scales the value so that the maximum haptic force

is provided when the trajectory is on the edge of the local UAV workspace. To remain consistent with the repulsive based feedback paradigm, the force sent to the haptic controller is scaled and translated to the \mathcal{H} frame

$$\vec{F}_h = k_{max}(R_{\mathcal{B}}^{\mathcal{H}} \cdot \vec{F}_a) \quad (2.10)$$

2.3.3 Combined Attractive and Repulsive Haptic Feedback

The third FFB mode is a linear combination of both the repulsive and attractive FFB algorithms. Each component of the overall haptic cue is calculated the same as the previous cases and combined according to

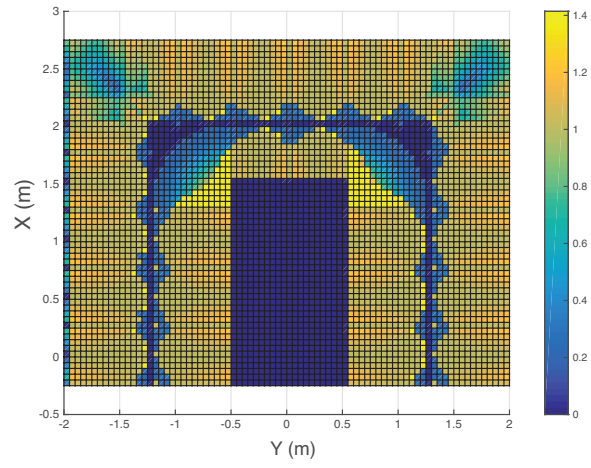
$$\vec{F}_h = k_{max}[\alpha \cdot \vec{F}_a + (1 - \alpha)\vec{F}_r] \quad , \quad 0 \leq \alpha \leq 1 \quad (2.11)$$

where α is a scaling term to appropriate the influences of each type of FFB vector. This scaling term is set to 0.5 to allow equal influence of attractive and repulsive FFB. The equal appropriation of each scheme is used to shed some light on contributions from each FFB modality. It is important to note that this singular parameter value creates an entirely different FFB scheme. Choice of the α parameter may contribute to a more appropriate or degraded FFB scheme but is used solely for comparative purposes here and adjustment of this parameter will be used in future studies.

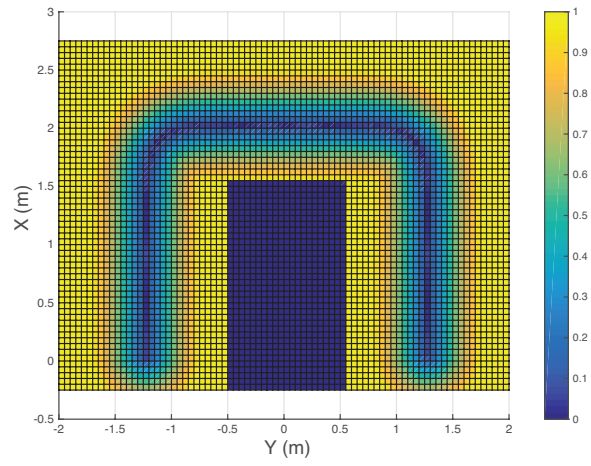
2.3.4 Feedback Overview

For brevity, the notation of attractive, repulsive, combined and no force feed back schemes, will be referred to as AF, RF, AF+RF, and NF respectively. For all three cases the FFB algorithms attempt to keep the UAV in the center of the corridor away from obstacles. While they all provide the least amount of FFB in the center of the path, differences can be seen in figure 2.2 which depicts the flight course used. For RF, shown in figure 2.2a, the magnitude of the haptic feedback has geometric constraints. This is most apparent near the corners of the flight course. By using a vector approach there is a cancellation that provides an overall force vector that is not truly representative of the surrounding environment. Analogously for AF, shown in figure 2.2b, this issue is resolved

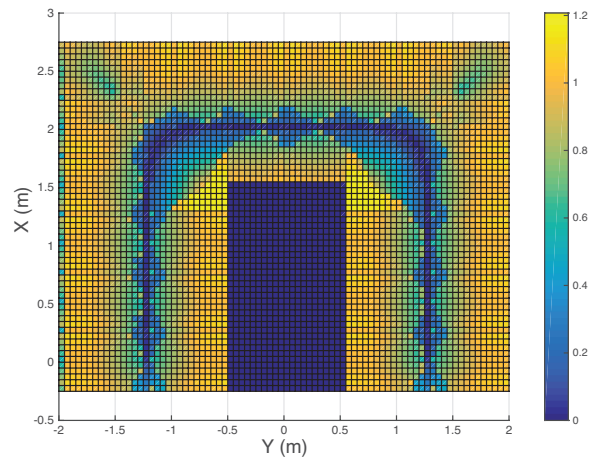
due to the force vector being isolated to a single geometric point. Another noticeable difference can be seen between RF and AF by observing the gradient profile of each. For RF there are sharp changes in the force magnitudes along the flight course. This is due to the change in the number of obstacles and their respective position in the local robot workspace. This suggests that the human operator will be provided with sharp changes in feedback cues during the experiment and will have a negative effect on their perception. For AF, there is a smooth change in the force magnitude over the flight course. This suggests that operating with AF will provide much smoother haptic cues to the operator.



(a) RF



(b) AF



(c) RF+AF

Figure 2.2: Gradient of force magnitudes along flight course.

Chapter 3

UAV Pilot Model Identification

This chapter explores a method by which accurate reconstruction of signals obtained during experimentation can be used to model lateral control efforts as a 1D tracking task. The simplest control model containing the human block is the black box architecture of the compensatory model depicted in figure 3.1 [37]. Compensatory behavior models the perception of instantaneous tracking error relying on the current state of the controlled element.

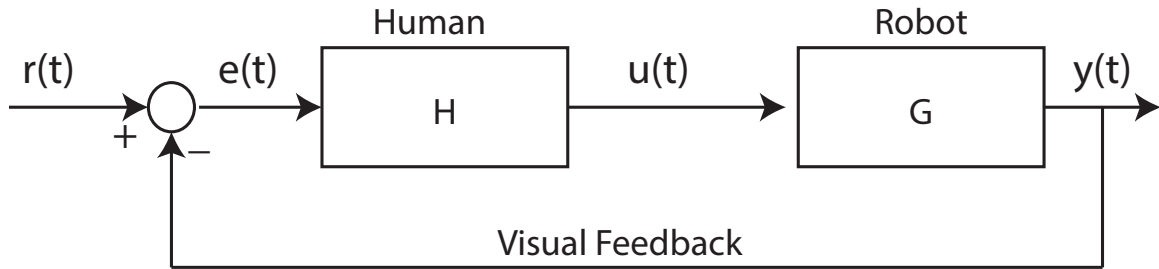


Figure 3.1: Control diagram for compensatory tracking

For identification of a human control model, compensatory behavior is considered due to the unpredictable nature of a reference signal. In a remote teleoperation task, the operator is only privy to visual information presented on a display yielding an associated human perceived error. Precognitive control can be excluded as the task is done remotely. Additionally, the choice of pure compensatory control over predictive models is based on the movement of the reference frame presented to the human where the error signal and reference signal would be the same. When haptic

force feedback is implemented into the system, the human operator receives additional sensory information transforming the control structure to that of figure 3.2.

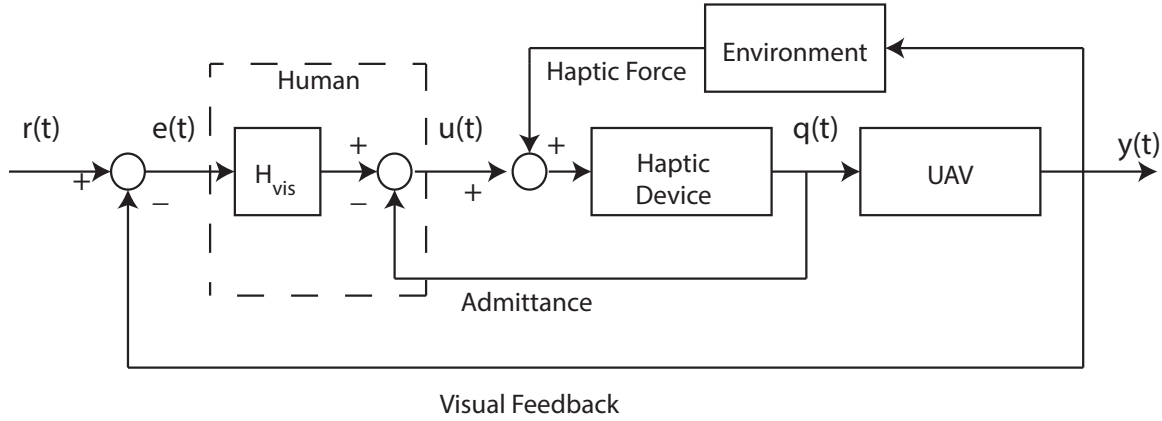


Figure 3.2: Control diagram including haptic aid.

With the introduction of haptic feedback into the system the human can be described as a two-input, single-output system. However, in [21], the authors state that a human cannot both receive force as an input and equally output an operational force. The additional input signal is then the neuromuscular response to the position of the haptic device. In [38], it is suggested that the human perceives haptic force feedback as a positional deflection of the control device having an effect on the human neuromuscular system. The neuromuscular system is further explained as the inverse of the arm admittance defined by the dynamic relationship between force and position [22]. The human control force is then a combination of the internal neuromuscular response and visual feedback represented by the H_{vis} block shown in figure 3.2.

3.1 Crossover Model

According to theories first described by McRuer [39], a human has the ability to internally adapt their control dynamics depending on the characteristics of the controlled element. Essentially, the human as a controller attempts to linearize the system within a limited frequency range centered around what is known as the crossover frequency ω_c . This crossover frequency is better defined as the frequency at which the open-loop transfer function from the error signal to system output is

unity. Accordingly, the open-loop transfer function defined, $HG_{ol}(j\omega)$, describes the lump human-plant dynamics near the crossover frequency, with time delay τ_v .

$$HG_{ol}(j\omega) = H(j\omega)G(j\omega) = \frac{\omega_c}{j\omega} e^{-j\omega\tau_v} \quad (3.1)$$

Here, $H(j\omega)$, and $G(j\omega)$ represent the human and controlled element respectively. The representation in equation (3.1) is known as the crossover model. According to this model, the open-loop transfer function will converge to that of a single integrator near ω_c . Once identified, the associated controlled element dynamics reveal characteristics of the human controller equalization. This model can further be extended to higher frequencies through the inclusion of the human neuromuscular system (NMS) often represented as:

$$H_{nms} = \frac{\omega_{nms}^2}{(j\omega)^2 + 2\zeta_{nms}\omega_{nms}j\omega + \omega_{nms}^2} \quad (3.2)$$

where ω_{nms} , and ζ_{nms} are the natural frequency and damping ratio respectively. The extended model suggests that a human operator will adopt lag compensation for a controlled element consisting of gain dynamics with lag time constant τ_{lag} . If the controlled element is explained by single-integrator dynamics, the human operator will adopt gain dynamics. For a controlled element of double-integrator dynamics the human operator will adopt lead compensation with associated lead time constant τ_{lead} . A summary of suggested human describing functions according to controlled element dynamics can be found in table 3.1. The first column shows a controlled element described by gain, single-integrator, and double-integrator dynamics with gain K_p . The second column shows the associated human describing function with gain K_h .

Controlled Element	Human Describing Function
K_p	$K_h e^{-\tau_v j\omega} H_{nms} / (\tau_{lag} j\omega + 1)$
$K_p / j\omega$	$K_h e^{-\tau_v j\omega} H_{nms}$
$K_p / (j\omega)^2$	$K_h e^{-\tau_v j\omega} H_{nms} (\tau_{lead} j\omega + 1)$

Table 3.1: Extended Crossover Model

The working principals of this section were adopted to this particular study to identify

human control with results presented in Chapter 6.

3.2 Operator Identification

For this study, a system with the architecture of figure 3.1 is considered for the non-haptic case while the architecture of figure 3.2 is considered for FFB schemes. The human component of the system is treated as a black-box model that describes the process of transferring input signals of visual error and haptic stimuli into force/position output signals fed back into the system. During experimentation, data was collected for the state of the UAV, human force, commands sent to the UAV and the feedback force provided by the haptic device. Using this data, signals were constructed to represent a reference point, and path error during flight. As the human operator controls the UAV without a direct line of sight, they must rely on the visual cues reported to them on the display in front of them. As the visual signal is projected onto a two-dimensional screen, depth perception is not quantifiable. Further reduction of flight into the horizontal plane allows for the current system identification to be reduced to that of a 1D tracking task of lateral motion.

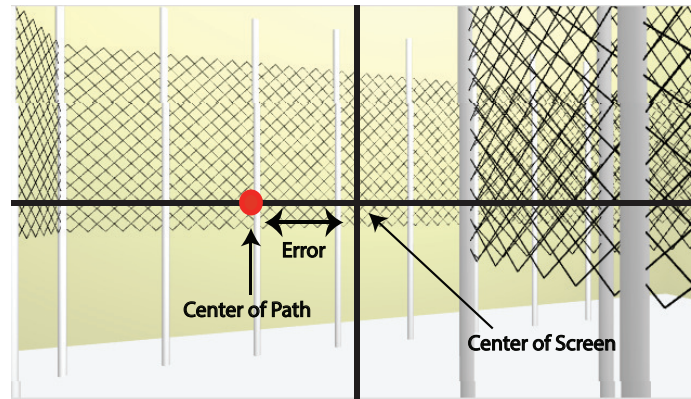


Figure 3.3: Human perception of error

One issue between identification of simulated tracking tasks and actual studies is the direct knowledge of error signals presented to the operator. To define an error signal that serves as input into the human block of the system consider figure 3.3. With vertical motion restricted, the operators perception of error is assumed to be interpreted as the deviation from the center of the current display screen to a target point in their field of view shown in figure 3.3. Corresponding control actions are

then an attempt to steer the UAV along the center of the track. The error signal $e(t)$ is then defined as the difference of the system output $y(t)$ (current position of the UAV, $X_r(t)$), and the reference signal $r(t)$ (current center of the virtual track) translated into the body frame.

$$e(t) = y(t) - r(t) \quad (3.3)$$

Having defined the error signal, the open-loop response of the overall system can be estimated from the closed-loop signals using spectral analysis. Defining $\hat{S}_{ry}(j\omega)$ and $\hat{S}_{re}(j\omega)$ as the cross spectral-densities between the reference signal, $r(t)$, the system output $y(t)$ and error $e(t)$.

$$\hat{H}G(j\omega) = \frac{\hat{S}_{ry}(j\omega)}{\hat{S}_{re}(j\omega)} \quad (3.4)$$

The analysis of $\hat{H}G(j\omega)$ will determine the validity of the crossover model if single integrator dynamics are present near the crossover frequency. Once the crossover model has been validated, similar spectral analysis can be used to estimate the human response function. According to the architecture of figures 3.1 and 3.2, the human output can be described by equation (3.5). The use of $H(j\omega)$ in equation (3.5) represents the human block as a combination of both the visual response as well as the neuromuscular response as it is not possible to accurately measure the admittance separately [22]. However, the effects of the neuromuscular response should still be captured as the measured human force will contain this information.

$$U(j\omega) = H(j\omega)E(j\omega) = H(j\omega)R(j\omega) - H(j\omega)Y(j\omega) \quad (3.5)$$

The Solving for $H(j\omega)$ and reducing to ratios of the reference signal yields:

$$H(j\omega) = \frac{U(j\omega)}{R(j\omega) - Y(j\omega)} = \frac{U(j\omega)/R(j\omega)}{(R(j\omega) - Y(j\omega))/R(j\omega)} = \frac{U(j\omega)/R(j\omega)}{E(j\omega)/R(j\omega)} \quad (3.6)$$

Therefore the estimated human response in the frequency domain is attained by

$$\hat{H}(j\omega) = \frac{\hat{S}_{ru}(j\omega)}{\hat{S}_{re}(j\omega)} \quad (3.7)$$

where $\hat{S}_{ru}(j\omega)$ is the cross spectral density of the reference signal and human force. For identification, the results of equation (3.4) and equation (3.7) along with controlled element dynamics will be used in Chapter 6 to first validate the use of the crossover model. After validation, controlled element dynamics can be used to help explain the results of equation (3.7).

Chapter 4

Experimental Design

To assess human behavior in a manual control flight task with haptic force feedback a test was designed where human subjects could remotely teleoperate a UAV along a course using a combination of visual and haptic aids.



Figure 4.1: Remote workspace providing only visual and haptic interfaces.

4.1 Physical Set Up

The chosen UAV was the Parrot AR.Drone 2.0 quad-rotor fitted with four pairs of active led markers. These markers were tracked in the 3D environment by a Phase Space tracking system including eight Impulse X2 cameras and a workstation. The human operator interfaces the system

by sitting at a work station containing a computer screen that provides the visual image captured by the forward facing camera on the UAV shown in figure 4.1. The human operator then manually controls the UAV through a 3-DoF Novint Falcon haptic feedback device. The experiment was implemented using a desktop computer running linux operating system using the Robotic Operating System (ROS)¹ as a middleware software updating at a rate of 20 Hz.

To represent an obstacle laden environment, a flight course shown in figure 4.2 was designed that simulates a corridor for a UAV to maneuver through that contains two right turns. The course consisted of 26 vertical poles spaced evenly throughout the maximum space provided by the tracking system covering a 4 m by 2.5 m rectangle. The use of vertical poles allowed ample visibility of the tracking system while also being constrictive enough to resemble walls. Each pole represented an obstacle for haptic force rendering and also serves as geometric constraints for reference trajectory generation.

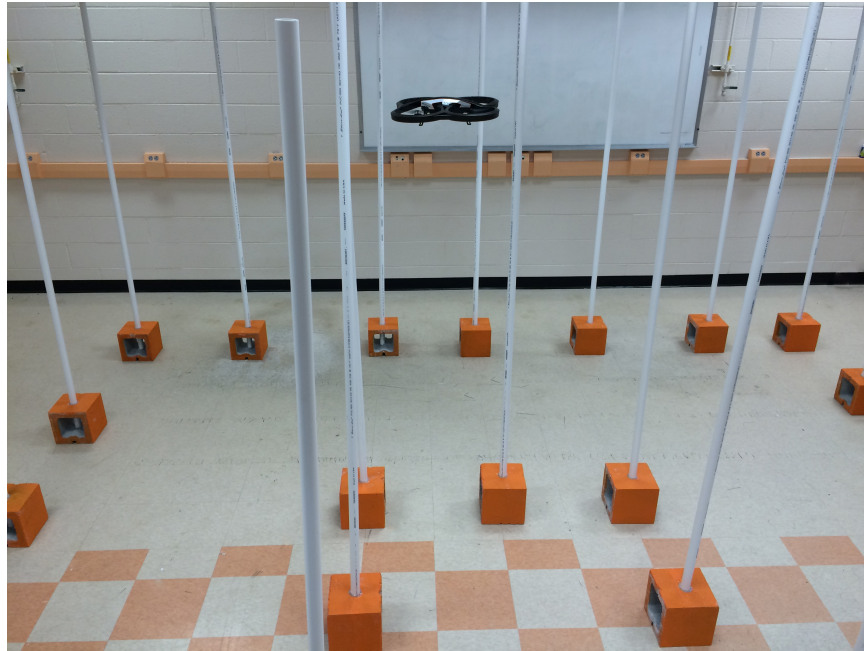


Figure 4.2: UAV flight track

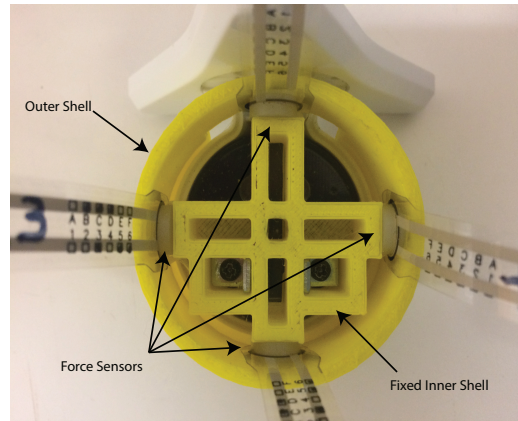
¹<http://ros.org>

4.2 Human Force Sensor

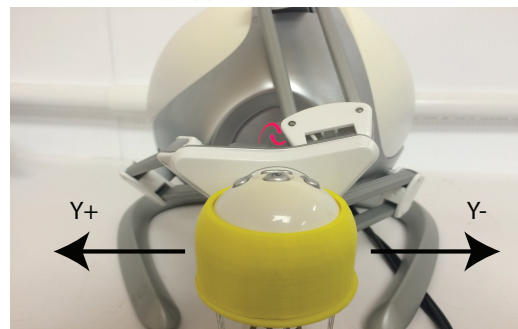
In order to attain the physical force output by the human, a device was made to measure axial forces and attached to the haptic device end effector. The bottom, top and front views of the created sensor array can be viewed in figure 4.3. The force measurement device consisted of an inner and outer hull that was 3D printed containing space for four resistive force sensors between the hulls. The inner hull was fixed to the end effector to provide a rigid surface for the sensors. The outer hull was free to move while maintaining a small internal force to keep the sensors properly placed. The force signals were measured by 8” FlexiForce 0-25 lb. Resistive Force Sensors made by Tekscan and fed through an analog to digital converter from Phidgets at a rate of 20 Hz. The sensors were placed in pairs representing the positive and negative horizontal planer positions of the end effector denoted as X^+ X^- , Y^+ , Y^- . The paired positions of the sensors provided accurate force sensing in both respective directions of movement along the lateral and longitudinal directions of motion. For simplicity, the notation of the end effector reference frame will assume the same as the UAV body. For example, if the human operator pushed to the left, there would be an increase in the output of Y^- and a decrease in the output of Y^+ . Similarly, if the operator pushed forward on the end effector, there would be an increase in the output of X^- and a decrease in the output of X^+ . The opposite is true for motion to the right and backward. As each participant held the device differently, calibration data was taken at the beginning of each trial. For this, participants moved the end effector to a position in each cardinal direction and paused to allow for data collection. The resulting force measured in the XY-plane can be represented as a linear combination of contributions from each sensor in the array as a function of time. This linear combination can then be equated to the measured internal force from the haptic device as

$$F_{lat}(t) = C_{1,lat}X^+(t) + C_{2,lat}X^-(t) + C_{3,lat}Y^+(t) + C_{4,lat}Y^-(t) + C_{5,lat} \quad (4.1)$$

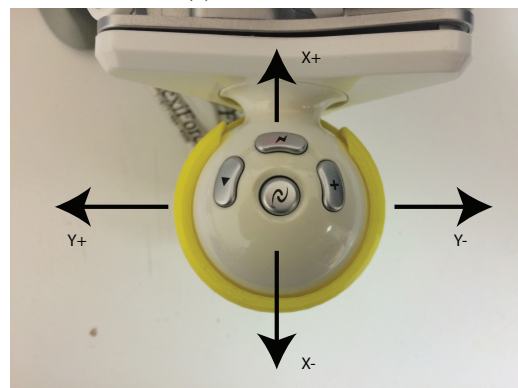
$$F_{long}(t) = C_{1,long}X^+(t) + C_{2,long}X^-(t) + C_{3,long}Y^+(t) + C_{4,long}Y^-(t) + C_{5,long} \quad (4.2)$$



(a) Bottom View



(b) Forward View



(c) Top down View

Figure 4.3: Force sensor array to record human-haptic interaction forces.

where $F_{lat}(t)$ and $F_{long}(t)$ represent the axial force produced by the haptic device and $C_{i,lat}$, $C_{i,long}$, $i = 1, \dots, 5$ are unknown constant coefficients of the linear model. In matrix form the general equation for both equations (4.1,4.2) where $l \in [lateral, longitudinal]$ can be represented as:

$$\begin{bmatrix} F_l(t_1) \\ F_l(t_2) \\ \vdots \\ F_l(t_n) \end{bmatrix} = \begin{bmatrix} X^+(t_1) & X^-(t_1) & Y^+(t_1) & Y^-(t_1) & 1 \\ X^+(t_2) & X^-(t_2) & Y^+(t_2) & Y^-(t_2) & 1 \\ \vdots & \vdots & \vdots & \vdots & \vdots \\ X^+(t_n) & X^-(t_n) & Y^+(t_n) & Y^-(t_n) & 1 \end{bmatrix} \begin{bmatrix} C_{1,l} \\ C_{2,l} \\ C_{3,l} \\ C_{4,l} \\ C_{5,l} \end{bmatrix} \quad (4.3)$$

more generally,

$$F_l = XC_l \quad (4.4)$$

To solve for the unknown coefficients the general solution to the normal equations can be used in equation (4.5).

$$C_l = (X^T X)^{-1} X^T F_l \quad (4.5)$$

Table 4.1 shows the average coefficient values found from equation (4.5) corresponding to equations (4.1) and (4.2). The presented values show that the influence of each force sensor was weighted appropriately for longitudinal and lateral directions. Note that the coefficient $C_{5,l}$ is a remnant fitting parameter not associated with any particular sensor but instead corrects for initial sensor values.

Orientation	Coefficient	Lateral	Longitudinal
X^-	$C_{1,l}$	-0.0374	0.2609
Y^+	$C_{2,l}$	-0.4988	-0.1316
X^+	$C_{3,l}$	0.1745	-0.4629
Y^-	$C_{4,l}$	0.6871	-0.1354
-	$C_{5,l}$	-2.0952	0.5317

Table 4.1: Average constant coefficients

By substituting the coefficients found in equation (4.5) into equations (4.1) and (4.2), the static model of human input force is achieved and denoted $F_{lat}^s(t)$, $F_{long}^s(t)$. However, during flight, dynamic effects must be compensated for. To correct for the dynamic case and to correctly assign

the correct direction of the human input force, the overall human force, $U_{h,l}$ is a combination of the haptic force and the static human force. The dynamic human forces, $U_{h,lat}(t)$ and $U_{h,long}(t)$ at time t , can be found by

$$U_{h,lat}(t) = -\left(|F_{lat}^s(t)| - |F_{lat}(t)|\right) \text{sgn}\left(F_{lat}(t)\right) \quad (4.6)$$

$$U_{h,long}(t) = -\left(|F_{long}^s(t)| - |F_{long}(t)|\right) \text{sgn}\left(F_{long}(t)\right) \quad (4.7)$$

An example of the calibrated human force can be found in figure 4.4. The plot shown was calibrated using the same data from both the internal force of the haptic device and the sensor array. The results show that the directional human-haptic forces can be resolved into lateral and longitudinal directions appropriately.

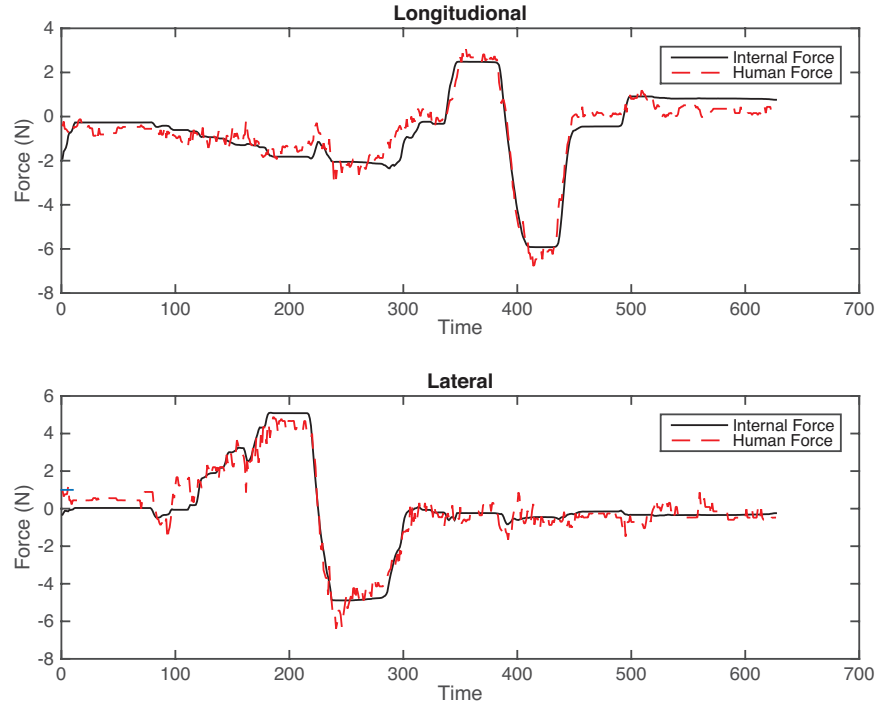


Figure 4.4: Calibrated human-haptic force

4.3 Procedure

Subjects were seated at a work station provided with a computer screen and haptic device. They were first instructed on how to operate the haptic device in reference to the UAV motion. Each subject was allotted a five minute period to practice flying with no FFB in a course that mirrored the testing course so that they did not learn how to fly a specific course. After the training period, participants were instructed that their task was to fly the UAV through the course as safely and efficiently as possible. They then piloted the UAV four times using the combination of visual feedback from the forward facing camera and each FFB mode. The four trials consisted of no FFB (NF), repulsive FFB (RF), attractive FFB (AF) and the combination (RF+AF). Each participant was provided with the FFB modes in different orders to control the learning effect. After the completion of each trial, subjects were given a performance and TLX survey.

Chapter 5

Performance Results

This chapter outlines the results pertaining to objective performance and subjective workload metrics as they pertain to two separate experiments. The first was implemented in a simulated environment using Gazebo¹. The simulated environment was modeled mimicking the physical lab and A.R. Drone quad-rotor in both dimension and dynamic characteristics. The second was a full scale experiment carried out in the physical lab. The simulation and full scale studies consisted of 17 and 28 participants respectively. Participant demographics can be found in appendix A. For both experiments, the haptic scaling factor K_{max} was set to 4, while the UAV workspace, r_w , and width r_{uav} were set to 0.5 m and 0.25 m respectively.

5.1 Flight Performance Metrics

To qualitatively compare FFB modes, a set of metrics are needed in order to measure flight performance. These proposed metrics seek to measure the ability of a teleoperator to navigate the UAV through the course both safely and efficiently. During the experiment, data was collected for the position and orientation of the UAV while performing the assigned flight task. For accuracy in comparison the data was filtered to only include flight after crossing a virtual starting line and finish line. This data was then used to calculate the following flight performance metrics.

¹<http://gazebosim.org>

Path Error (PE) is defined as the root mean square error (RMS) in the distance the UAV center of mass is from the center of the course. Obstacle Distance (OD) is calculated as the RMS distance the UAV center of mass is from an obstacle during flight task. The inclusion of both a path error and obstacle distance measure is to discredit the bias of the designed function between AF and RF. Completion Time (T) is the measurement of the length of time it took to complete the flight task. Finally, Path Length (PL) is the measurement of the total length of the UAV flight path between cutoff points.

5.2 Operator Workload Metrics

While performance metrics describe how well the flight task is performed, the implementation of FFB could have an adverse effect on how much effort is required by the pilot [40]. To assess this, two workload metrics were designed to measure operator workload for the task. The first is a subjective operator workload that is evaluated by NASA TLX² after each experiment. The second is a measure of operator's preference towards each FFB mode assessed via a post-test questionnaire with a 1-7 scale where 7 represented the highest preference.

5.3 Simulation Study

A simulation study was first conducted to achieve preliminary results of the feedback paradigm comparison. The main results of the experiment will be summarized here according to the metrics outlined above. During testing, four collisions with obstacles occurred from separate participants. Each FFB mode accounted for a single collision event and thus is not an appropriate metric for this study.

The results of all participants including the min, max, mean and std. dev. of each performance metric can be found in table 5.1. For clearer comparison figure 5.1 provides a histogram showing the average performance values side by side with the y-axis oriented to show favorable values on top. The average values for all tests are shown as a solid line while the dotted line represents

²<http://humansystems.arc.nasa.gov/groups/tlx/>

Path Error (cm)	Min	Max	Mean	Std
NF	13.98	31.25	21.26	5.41
RF	8.45	22.55	15.13	4.54
AF	7.24	28.47	15.55	6.26
RF+AF	8.24	25.29	16.78	5.18
OB Error (cm)	Min	Max	Mean	Std
NF	18.31	41.38	29.53	6.36
RF	26.16	46.53	36.53	6.66
AF	20.52	44.44	35.73	6.57
RF+AF	23.63	44.52	34.01	6.56
Time (sec)	Min	Max	Mean	Std
NF	7.60	35.60	15.40	6.50
RF	9.15	22.60	15.93	3.86
AF	9.45	29.30	17.26	4.66
RF+AF	9.00	24.55	15.90	3.80
Path Length (m)	Min	Max	Mean	Std
NF	4.15	6.65	4.93	0.69
RF	4.49	6.94	5.40	0.75
AF	4.22	7.73	5.55	0.89
RF+AF	4.27	6.79	5.34	0.78

Table 5.1: Performance metrics for simulated study

the PL of the reference trajectory. It can be seen that the AF and RF values are very close for each of the performance metrics. The case of NF shows a considerable disadvantage according to PE and OD with an advantage in PL and T. The PL and T metrics should be considered as a secondary measure for flight performance and only used to distinguish between cases where PE and OD are close. For example, a pilot can fly faster with a shorter distance but be dangerous in their maneuvers. This provides confirmation that there is a measurable improvement in flight performance though the use of haptic FFB with a 24-34% decrease in PE and a 14-21% increase of OD at the expense of only an increase of 8-11% and 3-11% in PL and T.

When comparing the results of RF and AF the percent difference for PE, OD, PL, and T was 2.78, 2.22, 2.78 and 8.04 respectively with RF favored in all cases. The corresponding results of an ANOVA test with repeated measures reveal that there is no statistical significance between RF and AF according to performance. However, after further examination of the forces provided through FFB, there is a noticeable difference between RF and AF. The average resultant force of RF

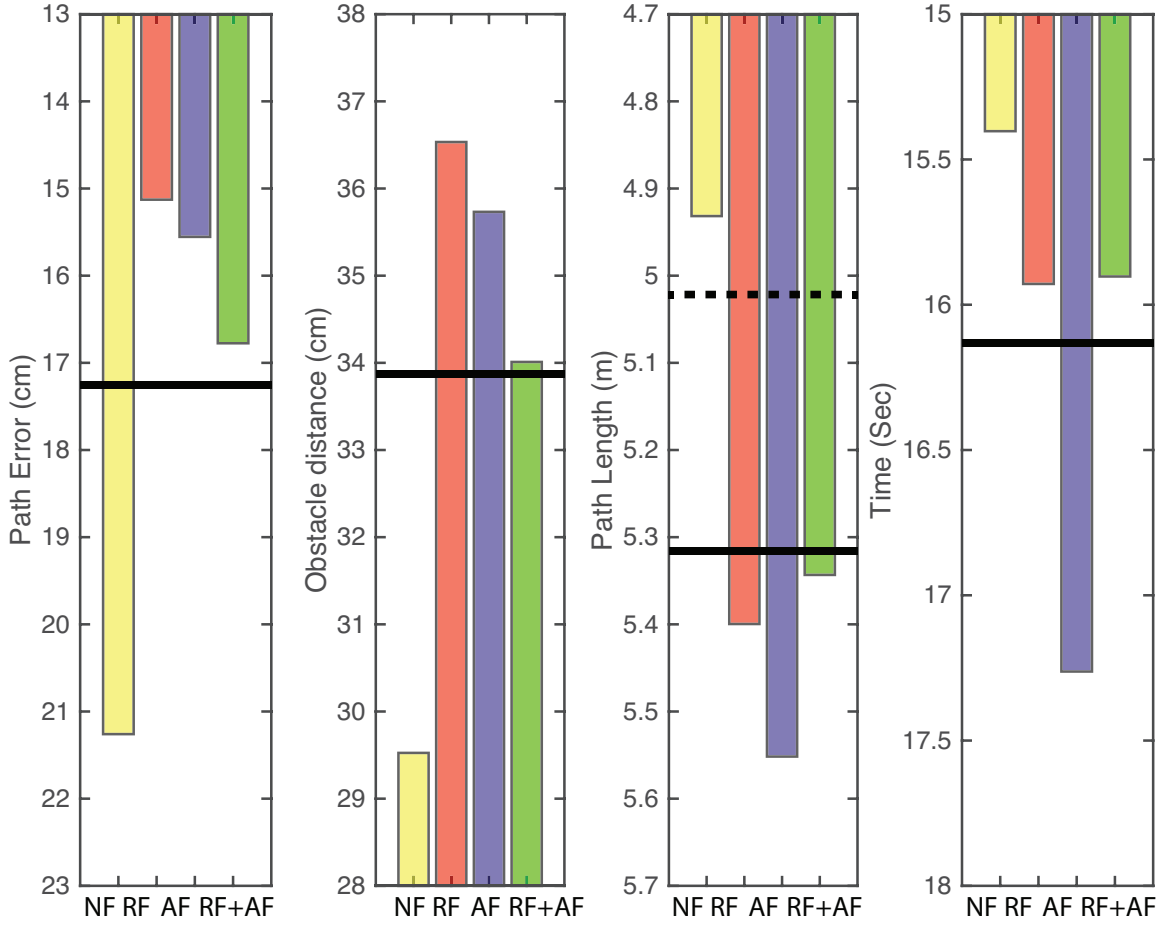


Figure 5.1: Means of performance metrics with higher vertical values representing more favorable values for NF (yellow), RF (red), AF (blue) and RF+AF (green).

and AF was 1.66N and 1.42N respectively. This represents a 15.5% ($p < 0.05$) higher average force when flying in RF mode.

Figure 5.2 illustrates an example of the forces provided to the operator for RF, AF and RF+AF, with the left column showing the force magnitude as a distribution over the haptic device workspace and the right column showing the total force over time. Looking at the distributions it can be seen that AF provides a more confined force distribution over RF and RF+AF. In figures 5.2b and 5.2f large rapid variations in force highlight the issues suggested in the introduction for obstacle avoidance FFB where the force provided to the operator is unstable due to the variability of obstacles in the local UAV workspace. In figure 5.2d some oscillatory effects from changing the closest point

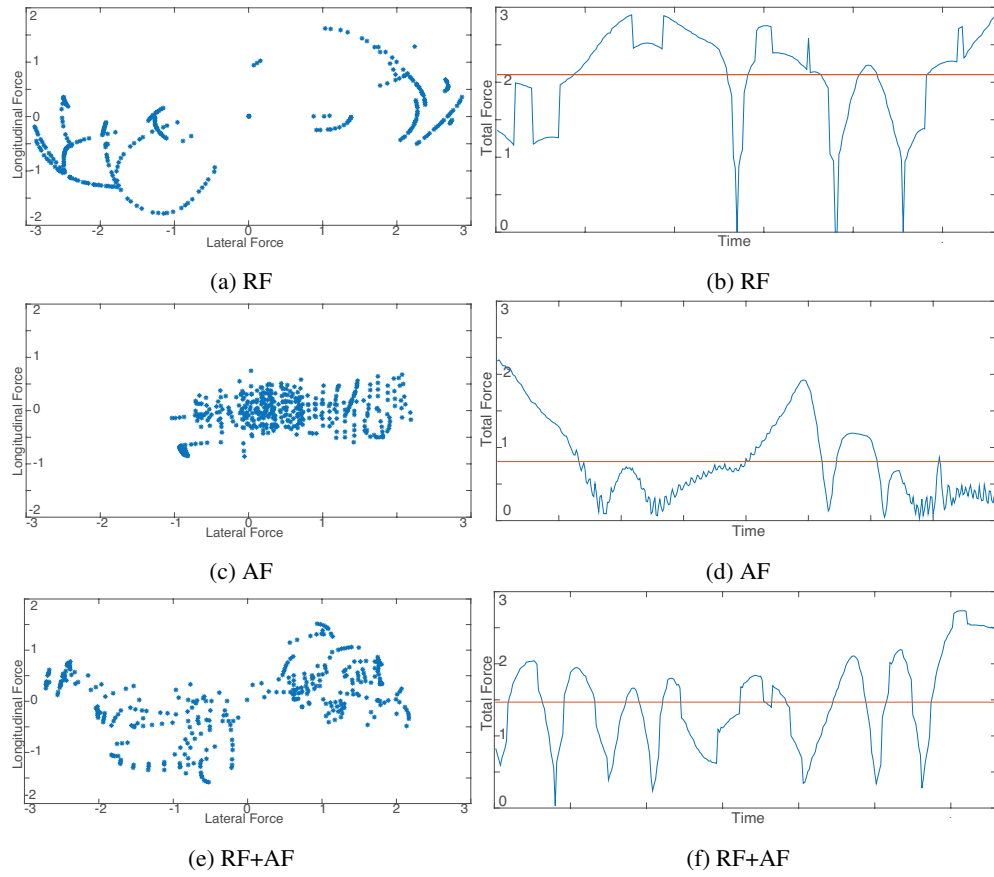


Figure 5.2: (a,c,e) Haptic force distribution represented in haptic device workspace; (b,d,f) Total haptic force over time with the horizontal line representing the average force.

on the reference trajectory are present, but this is only evident at lower forces with small variability and does not have an adverse effect on the smoothness of force over the entire flight path. These force results suggest the greatest differentiation between the case of RF and AF. While RF and AF produce the same performance, AF does so with a smoother FFB profile at lower force magnitudes.

For the case of RF+AF the average resultant force of 1.59N falls between RF and AF as a result of equal input from repulsive and attractive forces provided by equation 2.11. In figure 5.2f the force varies dramatically with sharp changes in maximum and minimum magnitude. This can be explained by the superposition of the RF and AF components. As the UAV deviates from the reference trajectory toward an obstacle it increases the force in both respects.

The results of the six workload metrics of the NASA TLX survey are shown in figures 5.3a-5.3g. Despite noticeable differences in effort and frustration between RF and AF the results did not show any statistically relevant effects for these measures.

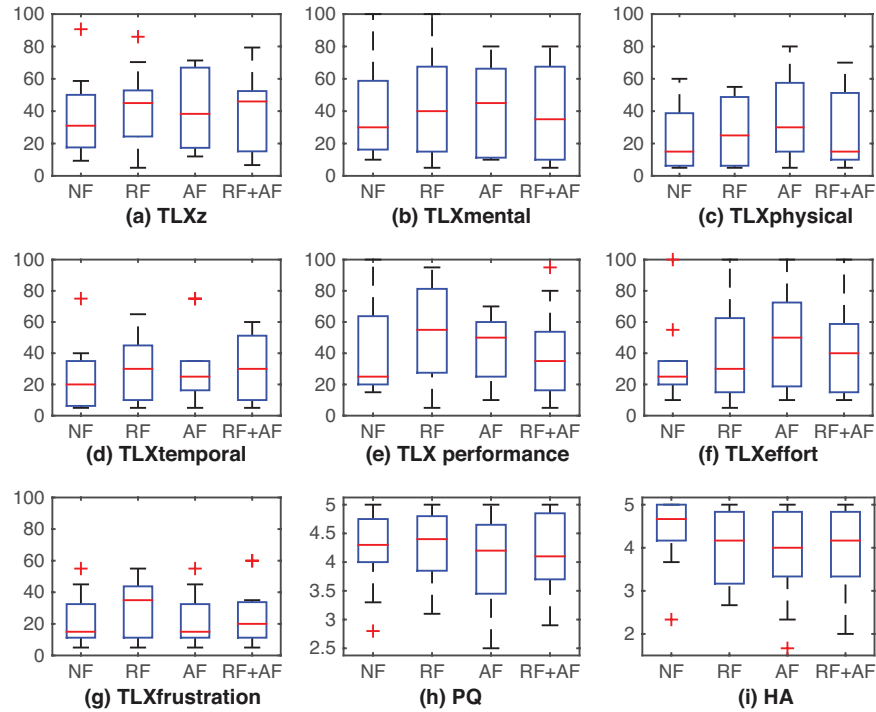


Figure 5.3: Medians and interquartile ranges of subjective metrics with outliers (+). PQ represents performance questionnaire and HA represents haptic acceptance.

It is important to note that the medians of frustration for RF, AF, and RF+AF in figure 5.3g

are consistent with the results above with respect to average force.

The performance questionnaire shown in figure 5.3h contained questions that repeated those of the TLX survey and confirm the TLX results. The responses in the questionnaire that pertained to control of the haptic device represented in figure 5.3h show that the addition of FFB did lower the operators preference for control but only by a small percentage. The results of the simulation study suggest that the performance and workload of both RF and AF feedback structures are similar. However, the difference in force profiles suggest that there should be a difference in either performance or workload metrics. To capture all dynamics of UAV flight and human workload perception, actual flight tests were implemented in an effort to expand simulation results.

5.4 Real Study

After the analysis of the simulation study a full scale study with actual UAV flight was conducted. The results of more test subjects and a tangible UAV with full flight dynamics should yield more realistic results. The main results of the experiment will be summarized here according to the metrics outlined above. After collection of data, samples that exhibited missing data in the form of packet drop from the tracking system or other recording fallacies were discarded to attain accurate results.

The results of all participants including the min, max, mean and std. dev. of each performance metric can be found in table 5.2. Again, for clearer comparison figure 5.4 provides a histogram showing the average performance values side by side with the y-axis oriented to show favorable values on top. The average values for all tests are shown as a solid line while the dotted line represents the PL of the reference trajectory.

By looking at the histogram, it can be seen that the case of AF yields the best results across all performance metrics. Behind AF, the case of RF+AF yields the second best results for these metrics. The metrics PE and OD found NF to yield the worst results while RF was found to have the worst results for PL and T. These findings are strengthened by the fact that the RF+AF results fall between the AF and RF values.

Path Error (cm)	Min	Max	Mean	Std
NF	18.43	46.58	33.85	8.20
RF	19.59	48.39	30.79	7.49
AF	15.69	35.16	26.35	5.29
RF+AF	14.29	49.79	28.86	8.76
OB Error (cm)	Min	Max	Mean	Std
NF	19.99	40.74	30.87	5.22
RF	20.68	40.15	32.13	4.80
AF	25.97	42.80	34.85	4.51
RF+AF	23.75	42.81	33.57	4.51
Time (sec)	Min	Max	Mean	Std
NF	6.60	36.70	15.25	7.37
RF	7.90	35.75	16.97	8.39
AF	7.15	25.95	12.35	5.73
RF+AF	5.85	37.65	14.53	7.90
Path Length (m)	Min	Max	Mean	Std
NF	4.97	9.96	6.98	1.52
RF	5.40	12.80	7.27	1.82
AF	4.83	10.32	6.71	1.57
RF+AF	4.20	13.91	6.75	2.15

Table 5.2: Performance metrics of real study

Based upon the results of an ANOVA test with repeated measures and Bonferroni correction between each test condition, AF produced a 24.9% ($p < 0.05$) and 12% ($p < 0.05$) increase in metrics PE and OD over NF. Also, AF had a 15.53% ($p < 0.05$) increase in PE over RF. For the PL metric the closest value for significance was an 8% ($p=0.20$) increase of AF over RF. Over all, there was an increase of 9.5 – 24.9%, 4.0 – 12.1% increase in PE and OD respectively for tests with haptic feedback over no haptic feedback that can conclude an increase in performance through the use of haptic cues. The differentiation between simulation and actual flight performance results reveal more than the effects of sample size. The simulation study represents a perfect control scenario where the virtual UAV reacts perfectly to control inputs. The actual flight results capture the full dynamics of the UAV that cannot be modeled in simulation. Due to the real flight capturing full dynamics of the UAV in an actual control setting, the results can be deemed more reliable and illustrate the importance of real experimentation.

The results of the six workload metrics of the NASA TLX survey are shown in figures

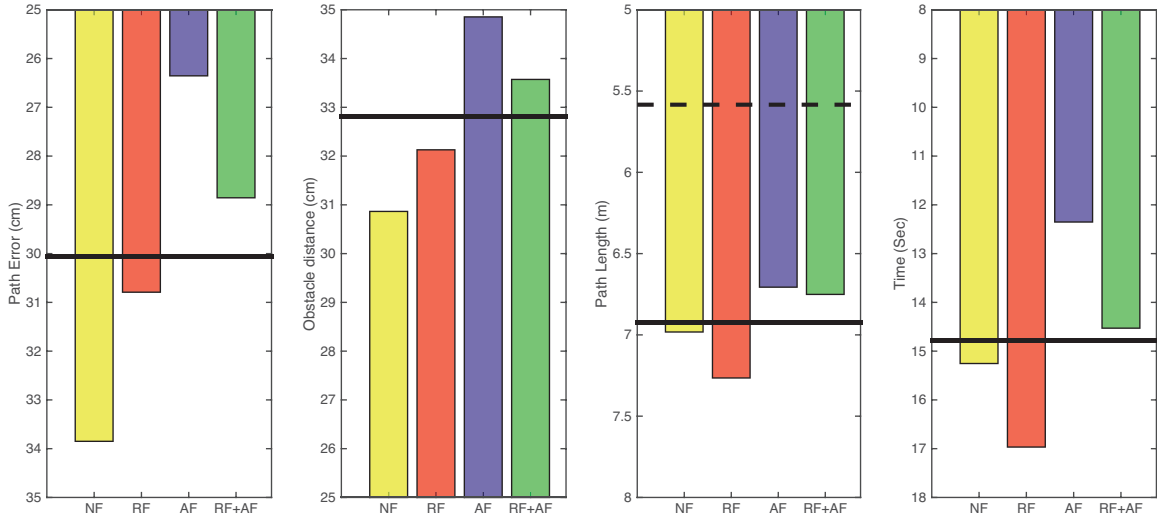


Figure 5.4: Means of performance metrics for real flight. NF (yellow), RF (red), AF (blue) and RF+AF (green).

5.5a-5.5g. Again using an ANOVA test with repeated measures and Bonferroni correction between each test condition again found no significant differences in human workload or human perception of performance. In fact, the only corresponding p-values that were not 1.00 were between RF and AF from the performance questionnaire with a p-value of $p = 0.290$. This suggests that the human perception of haptic feedback force when properly tuned is minimal as suggested [29] and [21]. However, it is important to note that the medians for all workload metrics follow the same trend as the performance metrics with AF showing the lowest workload, RF having the highest workload and RF+AF falling in the middle.

Side by side comparisons of the simulation and real study for workload metrics further contribute to an argument for full scale tests. The workload results for the real study are more contained with median values that are concentric about the 50% level. The more concise quartile ranges can be explained through sample size but there was an increase in workload across all measures. While none of these show maximum work load levels, the increase from the simulation to real study can only be explained by the inclusion of the actual UAV. It can be argued that humans show more concern for an actual device over a virtual object and their level of focus increased in real tests. Also, it is impossible to capture full dynamics of a UAV in simulation and therefore the operators had to

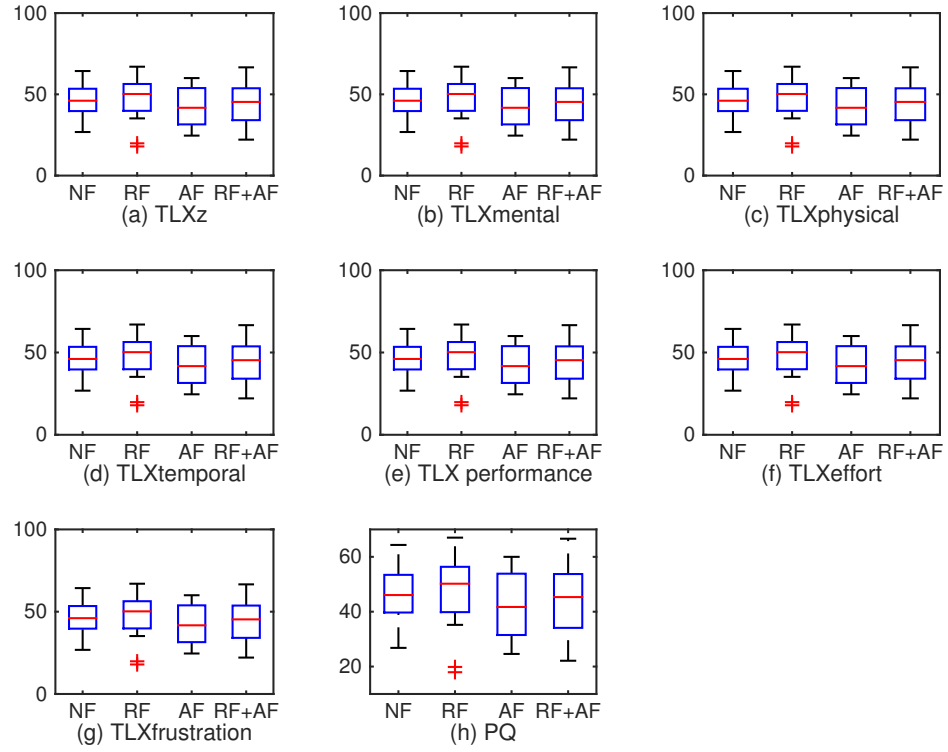


Figure 5.5: Medians and interquartile ranges of subjective metrics with outliers (+). PQ represents performance questionnaire and HA represents haptic acceptance.

work harder to compensate for these effects.

Chapter 6

Human Identification Results

The open-loop transfer function estimate $\hat{H}G(j\omega)$ shows the behavior of the human-machine system from the visual error presented to the operator to the position of the mobile robot. This includes the dynamics of the visual feedback, haptic device, haptic feedback, and mobile robot. Figure 6.1 shows the mean open-loop response of the lump system in the frequency domain for all feedback cases.

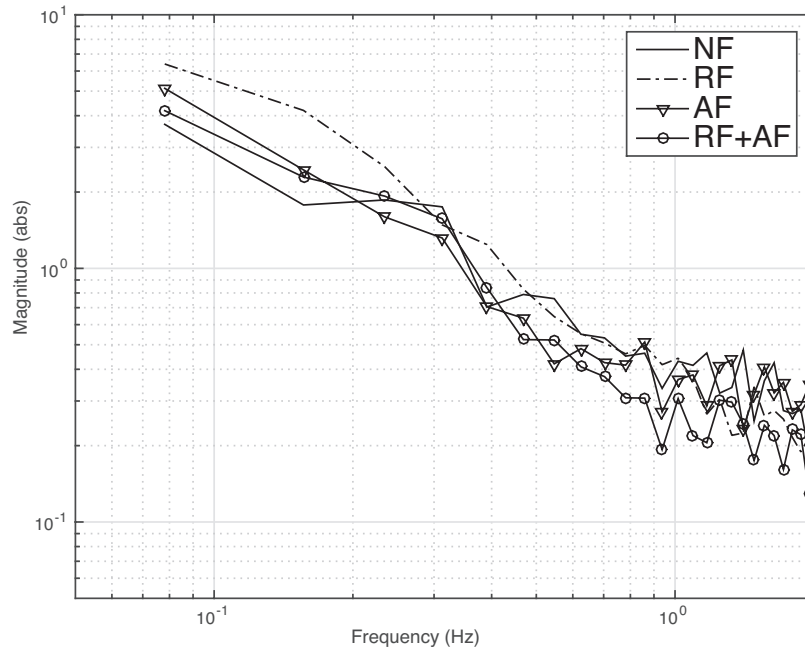


Figure 6.1: Estimated open-loop frequency response functions for all feedback conditions.

Based upon the widely accepted theories of McRuer, a human operator will alter their dynamics based upon the system that they control to achieve a lump pilot-vehicle model that can be approximated by a single integrator near the crossover frequency ω_c [41]. The slope of -1 for all four FFB schemes in figure 6.1 indicates that the open-loop estimates do exhibit single integrator behavior near the crossover frequency. This result validates that the crossover model holds and can be used to infer human behavior as a compensatory tracking task. Figure 6.2 presents the means and confidence regions of estimated crossover frequencies found through model fitting in Matlab. The difference in mean crossover frequency for RF is also highlighted by the apparent shift to the right present in figure 6.1. While this overall mean proved more compliant, further examination provided that there was no significance of the RF mean over other crossover estimates.

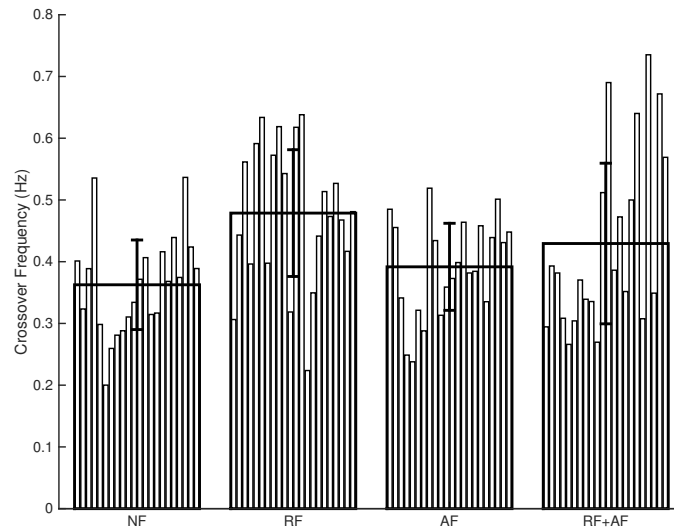


Figure 6.2: Means and 95% confidence intervals of the crossover frequency values.

Having determined that the human operator does change their behavior in order for the lump human-plant dynamics of a single integrator around the crossover frequency, the human model can be assessed based upon the dynamics of the mobile robot. To find UAV dynamics a post hoc test was performed. Controlled input commands over several ranges were sent to the UAV and its state was recorded. The resulting magnitude frequency response of the UAV is shown in figure 6.3. The bold dashed line at frequencies below 1 Hz has the corresponding transfer function of a pure double

integrator. The dash-dot line in figure 6.3 represents the single integrator in the form of equation (3.1) in the range of the estimated crossover frequencies. Referring back to Chapter 3, namely table 3.1 the human pilot generally equalizes a system with double integrator dynamics with a high lead term.

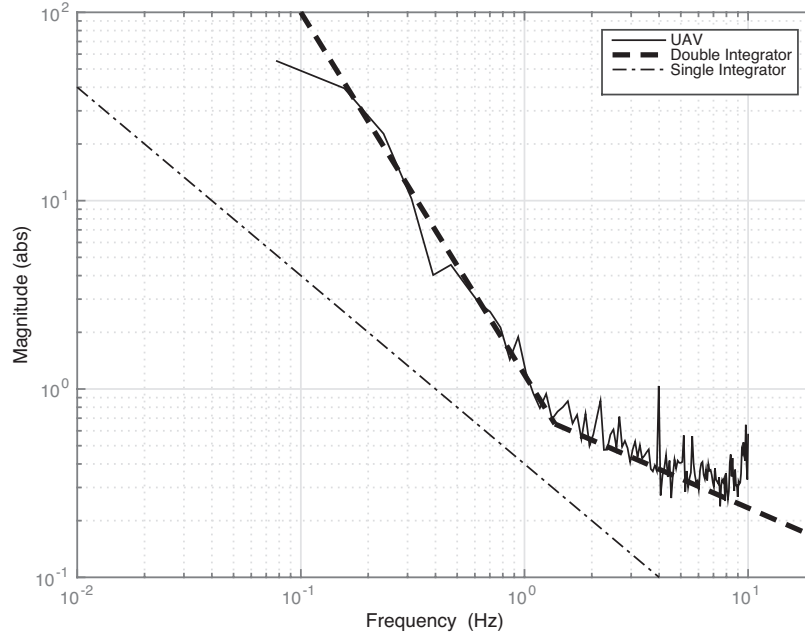


Figure 6.3: Mean UAV frequency response

Figure 6.4 shows the mean frequency response of human operators defined by equation (3.7). As suggested the human response exhibits behavior consistent with expected equalization behavior in all cases. The decrease in the amplitude at high frequencies for all FFB cases indicates neuromuscular system dynamics. For all cases shown in figure 6.4, there appears to be a drastic change near the crossover frequency range of 0.3-0.5 Hz. This increase from gain behavior suggests lead action in the form of $(1 + \tau_{lead}j\omega)$. The flattening and eventual decrease at higher frequencies exhibit second order lag dynamics consistent with that of the human neuromuscular system. Therefore human behavior for controlling the lateral dynamics of a UAV in a remote teleoperation task takes the form of

$$H(j\omega) = K_h e^{-\tau_v j\omega} H_{nms} (1 + \tau_{lead} j\omega) \quad (6.1)$$

which is consistent with previous literature as discussed in Chapter 3.

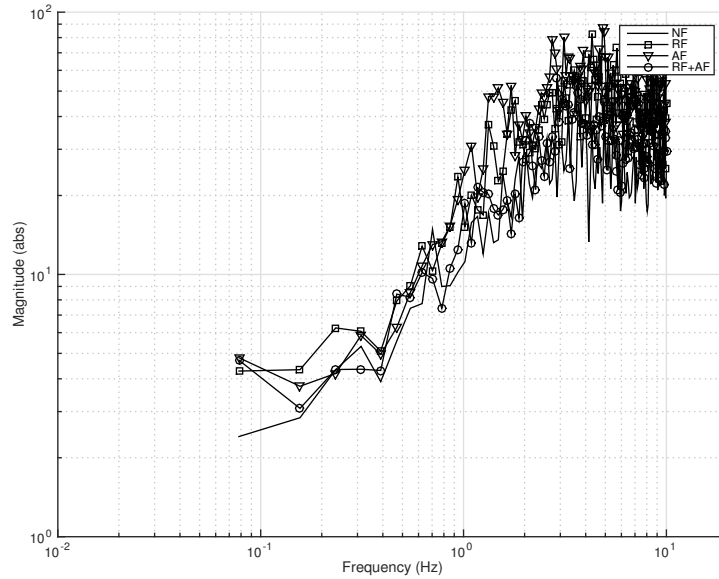


Figure 6.4: Mean human response estimates

As figure 6.4 suggests, the comparison of FFB schemes in the frequency domain is not feasible due to the resolution of the recorded data and differences between each specific participant. Recall, that the visual signal defined in Chapter 3 has room for error and contributes to this resolution deficiency. From this result, an improvement in performance for AF can only be explained by a change in the human visual response which is currently difficult to measure with absolute accuracy. Due to the similarity of all cases and neuromuscular effects being present at higher frequencies, results suggest that human control efforts are heavily dependent upon visual feedback. Due to resolution restraints, parameterization of human control efforts remain an open issue that can be clarified in future works. The most important result of this study however is that a human control model is in fact attainable with the current system setup and confirms that the crossover model holds when applied here.

Chapter 7

Conclusions and Discussion

With the continued involvement of human controllers in a control loop, information about how they react to the system is important. Through identification procedures, filters and adjustments can be added to the system in order to improve the performance of both the human and controlled element without degrading the human authority of the system. In this work the addition of haptic force feedback to improve flight performance was discussed. Namely the comparison of attractive and repulsive feedback models. Results found that an attractive force feedback scheme outperforms repulsive schemes in all performance measures. This result is strengthened by the performance results of the combination of both modalities falling between their respective results. The direct increase in human workload metrics between simulated and actual studies suggest that human control efforts should only be measured in real situations as the presence of all dynamics are present.

With actual experimentation, there are certain assumptions about human perception that must be made. Exploration of a method by which to define a humans perception of error was presented and validated through the crossover model. Results show that a human pilot of a remote UAV does invoke lead action to compensate for the second order dynamics of the piloted UAV near the crossover frequency while neuromuscular action takes over at higher frequencies. As significant differences between force feedback cases were negligible in system identification, the work presented here should serve as groundwork for further advancement into the identification of human control models for remote teleoperation of quadrotor unmanned aerial vehicles both with and without sup-

ported haptic force feedback. To better assess human control actions, future studies with increased space limitations allowing for longer flights with more configured parameters can lead to improved system identification.

Appendices

Appendix A Participant Demographics

The simulation study subjects consisted of 17 individuals that were willing participants offered no compensation. From a demographic questionnaire, 12 subjects were male and 5 female. The ages of participants consisted of 2 for 18-21, 4 were 22-24, 6 for 25-28 and 5 were over the age of 29. Among them 14 were students in engineering, 2 work in administration and 2 were students in another field. All but 5 participants listed themselves as active video game players and only 5 reported experience operating a UAV.

The full scale study consisted of 28 subjects under the same conditions of the simulation study where 20 were male and 8 were female. Their respective age ranges contained 2 for 18-21, 8 for 22-24, 8 for 25-28 and 10 over the age of 29. Among them 13 were students in an engineering field, 8 identified as other, 4 work in information technology, 2 were students in another field and 1 was a pilot. For video game usage, 12 reported that they do not play, 11 play occasionally, 4 play weekly and 1 plays daily. For joystick experience, 14 reported little or no experience, 12 had some experience and 2 are experienced using a joystick to control an object. Finally, all but 8 of the subjects reported no experience operating unmanned aerial vehicles.

Bibliography

- [1] T. Samad, J. S. Bay, and D. Godbole, “Network-centric systems for military operations in urban terrain: the role of uavs,” *Proceedings of the IEEE*, vol. 95, no. 1, pp. 92–107, 2007.
- [2] T. Pultarova, “Challenges of ‘dronevolution’ [news analysis],” *Engineering & Technology*, vol. 9, no. 12, pp. 16–17, 2014.
- [3] J. J. Cress, M. E. Hutt, J. L. Sloan, M. A. Bauer, M. R. Feller, and S. E. Goplen, “US geological survey unmanned aircraft systems (uas) roadmap 2014,” US Geological Survey, Tech. Rep., 2015.
- [4] R. Mahony, F. Schill, P. Corke, and Y. S. Oh, “A new framework for force feedback teleoperation of robotic vehicles based on optical flow,” in *Robotics and Automation, 2009. ICRA’09. IEEE International Conference on*. IEEE, 2009, pp. 1079–1085.
- [5] A. Kanso, I. H. Elhajj, E. Shammass, and D. Asmar, “Enhanced teleoperation of uavs with haptic feedback,” in *Advanced Intelligent Mechatronics (AIM), 2015 IEEE International Conference on*. IEEE, 2015, pp. 305–310.
- [6] U. Boschloo, T. M. Lam, M. Mulder, and M. Van Paassen, “Collision avoidance for a remotely-operated helicopter using haptic feedback,” in *Systems, Man and Cybernetics, 2004 IEEE International Conference on*, vol. 1. IEEE, pp. 229–235.
- [7] J. Cacace, A. Finzi, and V. Lippiello, “A mixed-initiative control system for an aerial service vehicle supported by force feedback,” in *Intelligent Robots and Systems (IROS 2014), 2014 IEEE/RSJ International Conference on*. IEEE, 2014, pp. 1230–1235.
- [8] X. Hou, R. Mahony, and F. Schill, “Comparative study of haptic interfaces for bilateral teleoperation of vtol aerial robots.”
- [9] E. Sunil, J. Smisek, M. M. van Paassen, and M. Mulder, “Validation of a tuning method for haptic shared control using neuromuscular system analysis,” in *Systems, Man and Cybernetics (SMC), 2014 IEEE International Conference on*. IEEE, 2014, pp. 1499–1504.
- [10] S. Stramigioli, R. Mahony, and P. Corke, “A novel approach to haptic tele-operation of aerial robot vehicles,” in *Robotics and Automation (ICRA), 2010 IEEE International Conference on*. IEEE, 2010, pp. 5302–5308.
- [11] A. Y. Mersha, S. Stramigioli, and R. Carloni, “Bilateral teleoperation of underactuated unmanned aerial vehicles: The virtual slave concept,” in *Robotics and Automation (ICRA), 2012 IEEE International Conference on*. IEEE, pp. 4614–4620.

- [12] P. Stegagno, M. Basile, H. H. Bulthoff, and A. Franchi, "A semi-autonomous uav platform for indoor remote operation with visual and haptic feedback," in *Robotics and Automation (ICRA), 2014 IEEE International Conference on*. IEEE, pp. 3862–3869.
- [13] T. M. Lam, H. W. Boschloo, M. Mulder, and M. M. Van Paassen, "Artificial force field for haptic feedback in uav teleoperation," *Systems, Man and Cybernetics, Part A: Systems and Humans, IEEE Transactions on*, vol. 39, no. 6, pp. 1316–1330, 2009.
- [14] H. I. Son, J. Kim, L. Chuang, A. Franchi, P. R. Giordano, D. Lee, and H. H. Bülthoff, "An evaluation of haptic cues on the tele-operator's perceptual awareness of multiple uavs' environments," in *World Haptics Conference (WHC), 2011 IEEE*. IEEE, 2011, pp. 149–154.
- [15] A. M. Brandt and M. B. Colton, "Haptic collision avoidance for a remotely operated quadrotor uav in indoor environments," in *Systems Man and Cybernetics (SMC), 2010 IEEE International Conference on*. IEEE, 2010, pp. 2724–2731.
- [16] T. M. Lam, H. W. Boschloo, M. Mulder, M. Van Paassen, and F. Van der Helm, "Effect of haptic feedback in a trajectory following task with an unmanned aerial vehicle," in *Systems, Man and Cybernetics, 2004 IEEE International Conference on*, vol. 3. IEEE, pp. 2500–2506.
- [17] S. Omari, M.-D. Hua, G. Ducard, and T. Hamel, "Bilateral haptic teleoperation of vtol uavs," in *Robotics and Automation (ICRA), 2013 IEEE International Conference on*. IEEE, 2013, pp. 2393–2399.
- [18] S. Lee, G. S. Sukhatme, G. J. Kim, and C.-M. Park, "Haptic control of a mobile robot: A user study," in *Intelligent Robots and Systems, 2002. IEEE/RSJ International Conference on*, vol. 3. IEEE, 2002, pp. 2867–2874.
- [19] J. G. Wildenbeest, R. J. Kuiper, F. C. van der Helm, and D. A. Abbink, "Position control for slow dynamic systems: Haptic feedback makes system constraints tangible," in *2014 IEEE International Conference on Systems, Man, and Cybernetics (SMC)*. IEEE, 2014, pp. 3990–3995.
- [20] H. I. Son, A. Franchi, L. L. Chuang, J. Kim, H. H. Bulthoff, and P. R. Giordano, "Human-centered design and evaluation of haptic cueing for teleoperation of multiple mobile robots," *Cybernetics, IEEE Transactions on*, vol. 43, no. 2, pp. 597–609, 2013.
- [21] E. A. Y. Murakami, K. Shibata, X.-Z. Zheng, and K. Ito, "Human control characteristics in bilateral micro-teleoperation system," in *Industrial Electronics Society, 2000. IECON 2000. 26th Annual Conference of the IEEE*, vol. 1. IEEE, 2000, pp. 602–607.
- [22] M. Olivari, F. M. Nieuwenhuizen, J. Venrooij, H. H. Bülthoff, and L. Pollini, "Multi-loop pilot behaviour identification in response to simultaneous visual and haptic stimuli," in *AIAA Modeling and Simulation Technologies Conference*, 2012, p. 4795.
- [23] D. T. McRuer and H. R. Jex, "A review of quasi-linear pilot models," *IEEE Transactions on Human Factors in Electronics*, no. 3, pp. 231–249, 1967.
- [24] D. McRuer and D. H. Weir, "Theory of manual vehicular control," *Ergonomics*, vol. 12, no. 4, pp. 599–633, 1969.

- [25] J. Smisek, M. van Paassen, M. Mulder, and D. A. Abbink, "Neuromuscular analysis based tuning of haptic shared control assistance for uav collision avoidance," in *World Haptics Conference (WHC), 2013*. IEEE, 2013, pp. 389–394.
- [26] E. Itoh and S. Suzuki, "Nonlinear approach for human internal models: Feedforward and feedback roles in pilot maneuver," in *2005 IEEE International Conference on Systems, Man and Cybernetics*, vol. 3. IEEE, 2005, pp. 2455–2462.
- [27] B. Yu, R. B. Gillespie, J. S. Freudenberg, and J. A. Cook, "Human control strategies in pursuit tracking with a disturbance input," in *53rd IEEE Conference on Decision and Control*. IEEE, 2014, pp. 3795–3800.
- [28] L. B. Palma, F. V. Coito, and P. S. Gil, "Low order models for human controller-mouse interface," in *2012 IEEE 16th International Conference on Intelligent Engineering Systems (INES)*. IEEE, 2012, pp. 515–520.
- [29] L. F. Peñín, A. Caballero, R. Aracil, and A. Barrientos, "Human behavior modeling in master-slave teleoperation with kinesthetic feedback," in *Robotics and Automation, 1998. Proceedings. 1998 IEEE International Conference on*, vol. 3. IEEE, 1998, pp. 2244–2249.
- [30] M. Innocenti, A. Balluchi, and A. Balestrino, "New results on human operator modelling during nonlinear behavior in the control loop," in *American Control Conference, 1997. Proceedings of the 1997*, vol. 4. IEEE, 1997, pp. 2567–2570.
- [31] K. van der El, D. M. Pool, H. J. Damveld, M. M. van Paassen, and M. Mulder, "An empirical human controller model for preview tracking tasks," 2015.
- [32] F. M. Drop, D. M. Pool, H. J. Damveld, M. M. van Paassen, and M. Mulder, "Identification of the feedforward component in manual control with predictable target signals," *IEEE transactions on cybernetics*, vol. 43, no. 6, pp. 1936–1949, 2013.
- [33] D. M. Pool, P. M. Zaal, H. J. Damveld, M. M. van Paassen, and M. Mulder, "Pilot equalization in manual control of aircraft dynamics," in *Systems, Man and Cybernetics, 2009. SMC 2009. IEEE International Conference on*. IEEE, 2009, pp. 2480–2485.
- [34] V. A. Laurensse, D. M. Pool, H. J. Damveld, M. R. M. van Paassen, and M. Mulder, "Effects of controlled element dynamics on human feedforward behavior in ramp-tracking tasks," *IEEE transactions on cybernetics*, vol. 45, no. 2, pp. 253–265, 2015.
- [35] M.-D. Hua, T. Hamel, P. Morin, and C. Samson, "A control approach for thrust-propelled underactuated vehicles and its application to vtol drones," *Automatic Control, IEEE Transactions on*, vol. 54, no. 8, pp. 1837–1853, 2009.
- [36] L. Biagiotti and C. Melchiorri, *Trajectory planning for automatic machines and robots*. Springer Science & Business Media, 2008.
- [37] X. Zhang, T. Seigler, and J. B. Hoagg, "Modeling the control strategies that humans use to control nonminimum-phase systems," in *2015 American Control Conference (ACC)*. IEEE, 2015, pp. 471–476.

- [38] T. M. Lam, M. Mulder, and M. M. van Paassen, “Haptic interface in uav tele-operation using force-stiffness feedback,” in *Systems, Man and Cybernetics, 2009. SMC 2009. IEEE International Conference on*. IEEE, 2009, pp. 835–840.
- [39] D. T. McRuer, “Human pilot dynamics in compensatory systems,” DTIC Document, Tech. Rep., 1965.
- [40] J. Andersh, B. Mettler, and N. Papanikolopoulos, “Experimental investigation of teleoperation performance for miniature rotorcraft,” in *Decision and Control, 2009 held jointly with the 2009 28th Chinese Control Conference. CDC/CCC 2009. Proceedings of the 48th IEEE Conference on*. IEEE, 2009, pp. 6005–6010.
- [41] D. T. McRuer, D. Graham, and I. Ashkenas, *Aircraft dynamics and automatic control*. Princeton University Press, 2014.